



## Blind de-convolution of images degraded by atmospheric turbulence

Gongping Chen, Zhisheng Gao\*, Qiaolu Wang, Qingqing Luo

School of Computer and Software Engineering, Xihua University, Chengdu 610039, PR China



### ARTICLE INFO

#### Article history:

Received 21 June 2019

Received in revised form 27 December 2019

Accepted 23 January 2020

Available online 31 January 2020

#### Keywords:

Convolutional autoencoder

Asymmetric U-net

Space target image

Blind restoration

Atmospheric turbulence

### ABSTRACT

Atmospheric turbulence can change the path and direction of light during the imaging of a target in space due to the random motion of the turbulent medium, resulting in severe image distortion. To correct geometric distortion, and reduce spatially and temporally varying blur, this paper proposes a convolutional network for blind deblurring atmospheric turbulence (BDATNet) that includes a feature extraction noise suppression block (FENSB), an asymmetric U-net, and an image reconstruction subnetwork (IRSubnetwork). A deblurring noise suppression block (DNSB) is used instead of the traditional convolution layer for the U-net. The core principle of this model is to suppress noise before deblurring. During convolutional encoding, the FENSB and DNSB can suppress noise and capture rich feature maps. To fuse information obtained from low-level and high-level features, the FENSB and IRSubnetwork are skip-connected to ensure the integrity of the former during image reconstruction. Moreover, the method of gradually increasing the difficulty of data to train the network is used to cause it to gradually converge from simple to complex, so that it can deal with images severely degraded by turbulence. The experimental results of real data and simulation data show that the BDATNet can restore details of the image and sharpen its edges, and can suppress noise.

© 2020 Elsevier B.V. All rights reserved.

### 1. Introduction

The atmosphere is the medium of transmission for any optical system. If the exposure time is not short enough, the refractive index along the path of optical transmission can significantly affect the performance of the remote imaging systems, leading to geometric distortion, de-focused blur, and motion blur [1–5]. Therefore, eliminating the influence of atmospheric turbulence from images is crucial for remote imaging systems (ground based and space based) [6,7]. Ground-based space target imaging is particularly susceptible to ground gas, stray light, high-energy particles, and nebula interference coupled with severe thermal and electronic noise. The result is a significant degradation and low signal-to-noise ratios (SNRs) of images obtained by the imaging system [8,9]. Methods for restoring images of targets in space can be divided into two categories, real-time detection, and compensation sensors and digital image processing after imaging [10]. However, hardware-based adaptive optics can correct only part of the turbulent distortion because it is prone to various errors. In applications, atmospheric turbulence has complex point-spread functions (PSFs) whose shapes change with time and the overall field of view [11,12]. Restoring blurred images using digital image processing technology has long been a popular subject of research. We focus here on the problem of removing blur due

to atmospheric turbulence from a single image, based on the assumption that a blurred image  $f$  can be generated by linearly transforming the underlying image  $g$  (sometimes called the true image or latent image) by a convolution (denoted by  $*$ ), and adding noise  $n$ . The last decade has seen continual progress in research on removing blur in images owing to atmospheric turbulence, and many methods have been proposed to this [13–17]. Such post-processing calculations that improve the resolution of the image can be modeled as an ill-posed inverse problem:

$$f = g * h * k + n, \quad (1)$$

where  $g$  is the true image,  $k$  and  $h$  are the PSFs of geometric deformation and atmospheric turbulence, respectively,  $n$  represents additive noise, and  $f$  is the observed image [13]. Many methods have obtained highly precise estimates  $\hat{g}$  of the real image  $g$  such as the inverse filter-based method [18], feature learning-based method [19], total variation-based method [20], wavefront estimation-based method [21,22], and Bayesian methods [23]. However, most of these methods are suitable only for restoring images with a single degradation that is not severe (such as motion blur). In applications, images of spatial target are often affected by multiple degradation factors, and the above methods struggle to achieve the desired effect in this case [24].

Deep neural networks have powerful feature learning capabilities [19], and have achieved remarkable success in advanced visual tasks as well as low-level visual tasks, such as image restoration [25–29], denoising [30–32], JPEG artifact reduction [33–35]

\* Corresponding author.

E-mail address: [gzs\\_xihua@mail.xhu.edu.cn](mailto:gzs_xihua@mail.xhu.edu.cn) (Z. Gao).

and super-resolution [36–40]. Deep learning has provided new ideas for the restoration of images of targets in space. This paper focuses on the use of neural networks for this purpose. Images of targets in space may be degraded due to a variety of factors; as such, it is difficult to achieve the desired effect using only a simple neural network. Most blind de-noising approaches for images consist of two stages, i.e., noise estimation and non-blind de-noising. Several sophisticated noise models, e.g., the correlated Gaussian model [41,42], signal and frequency dependent noise model [43,44], and Poisson–Gaussian noise model [45], have been developed. This paper proposes the idea of first removing a few factors that degrade images and then removing the rest of them to obtain clear images. Moreover, neural networks based on end-to-end training methods have been widely studied and applied, and have achieved competitive results in image restoration in recent years [19,28]. Motivated by the above methods and characteristics of degraded images of spatial targets, this paper proposes a convolutional neural network model for the blind deblurring of images blurred by atmospheric turbulence (BDATNet) that consists of a stacked FENSB, an asymmetric U-net, and an image reconstruction subnetwork (IRSubnetwork). We develop a high-performance deep CNN model for the blind deblurring of images degraded by atmospheric turbulence that is robust. The main contributions of this paper are as follows:

(1) For images affected by atmospheric turbulence, this paper designs a convolutional BDATNet by incorporating network architecture, stacked FENSB, asymmetric U-net, and an IRSubnetwork. The FENSB and IRSubnetwork extract features from the input image while suppressing noise and reconstruct images based on the features acquired after removing atmospheric turbulence, respectively.

(2) The FENSB and IRSubnetwork are used for skip-connections as well to ensure that the feature map used for reconstructing the image has more information on the original image. The feature map extracted by the FENSB merged with the input image is taken as the input to the asymmetric U-net network, which improves the de-noising and deblurring performance of BDATNet.

(3) The FENSB block and DNSB are used to suppress different levels of noise and improve the de-noising performance of BDATNet.

(4) Training datasets with different degrees of degradation and difficulty of restoration were simulated. A method whereby the difficulty of the training data was gradually increased was used to train the network, to cause it to gradually converge from simple to complex.

## 2. Related work

In cases where images of the spatial target are severely degraded, the traditional method of blind restoration based on iterative optimization struggles to obtain good results [46]. To better observe the target, on the one hand, it is important to improve the accuracy of adaptive optics (AO) [47–51] and, on the other, machine learning methods are needed to improve the quality following AO. Methods based on AO have the advantages of clear principles and good interpretation, but the disadvantages of expensive equipment, and a failure to completely overcome the effects of turbulence and noise. Learning-based methods, especially those based on deep neural networks, have significant advantages over traditional methods in terms of speed and restoration performance [52].

Deep neural network-based methods can be used to estimate the waveform of distortion due to atmospheric turbulence. Gomez et al. [53] developed a technology for solar observation based on artificial neural network technology, and Jin et al. [54] proposed a joint technique for the detection and adaptive demodulation of atmospheric turbulence based on the convolutional

neural network for OAM-based free-space optics communication. The deep noise reduction convolutional neural network was introduced to phase diversity image preprocessing to defocus in-focus images and those containing Gaussian white noise to improve the robustness of PD to noise [55].

The direct blind deconvolution of the AO output image using a deep neural network can improve its quality. Ramos et al. [56] used a deep learning technique to accelerate blind deconvolution, and proposed two architectures that provide excellent image correction and noise suppression while maintaining the photometric properties of the image. But this method is still in the stage of theoretical development. Gao et al. [46] proposed a convolution auto-encoder for the blind deconvolution of single-frame images of targets in space. This method applies a convolutional auto-encoding neural network to the blind restoration of images of spatial targets to deliver impressive restoration performance. However, the network is too simple to fully and accurately learn features of the target image.

Deep neural networks have also been studied for the restoration of natural images, and the relevant methods have helped inspire this study. A deep convolutional neural network was used to capture the characteristics of degradation [57]. Hradis et al. found that highly structured data can be successfully restored by convolutional neural networks [58]. This method is sensitive to the orientation of the page, font style, and the language of the text, and has achieved good results [59]. Mao et al. used deep convolutional encoder–decoder networks with symmetric skip connections for image restoration [60]. Zhang et al. [61] removed noise from the gradient domain by training a full convolutional neural network (FCNN), and used the learning gradient method to guide image de-convolution. A multi-scale convolutional neural network that can restore sharp images in an end-to-end manner, where blur is caused by various sources, has been proposed [25]. The generative adversarial network has also been used for blind motion deblurring [62]. Guo et al. used the estimated noise map as input to directly remove noise from the degraded image [32], and Zhang et al. used an end-to-end, trainable, spatially variant RNN for dynamic deblurring of scenes [29].

## 3. Proposed method

### 3.1. Motivation

Images of spatial targets obtained using a ground-based telescope have a degradation pattern different from that of the datasets of images used in most prevalent studies in the area. Many image reconstruction algorithms for images of objects in space are based on the ideal linear model given by [63]:

$$f(x, y) = g(x, y) * h(x, y) + n(x, y), \quad (2)$$

where  $*$  is the convolution operation,  $h(x, y)$  is the PSF of atmospheric turbulence, and  $n(x, y)$  is the noise function, which is often regarded as Gaussian noise. However, the images of spatial targets are affected by a variety of degenerative factors. The process of multi-factor coupling degradation can be expressed as follows [46]:

$$f(x, y) = O(g(x, y) * h(x, y) * k(x, y) + \xi(x, y)) + n(x, y), \quad (3)$$

where  $n(x, y)$  is the noise of the sensor system,  $\xi(x, y)$  is the noise of transmission of the image of the target in space,  $h(x, y)$  is the PSF of atmospheric turbulence,  $k(x, y)$  is the PSF of geometric distortion, and  $O(\cdot)$  denotes the adaptive optics correction. It is evident that the image of the spatial target is affected by atmospheric turbulence blur as well as a variety of noises. Severe noise interference is a unique difficulty in images of spatial targets.

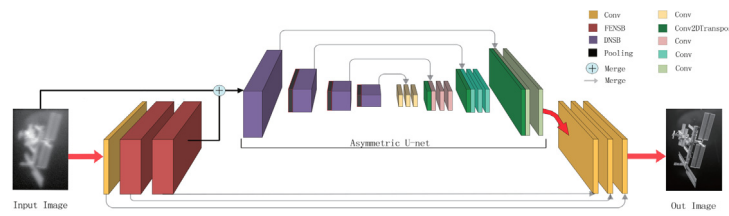


**Fig. 1.** Structure of BDATNet. It consists of a convolutional layer, two groups of FENSB, an asymmetric U-net, and an IRSUBnetwork. The activation function used is ReLU.

**Table 1**  
Configurations of the BDATNet.

Layer	Conv1	Staked FENSB		Asymmetric U-net	IRSubnetwork		
		FENSB	FENSB		Conv25	Conv26	Conv27
Filter size	3	\	\		3	3	3
Merge	\	\	\		Conv5	Conv3	Conv1

**Table 2**  
Configurations of the FENSB.

Layer	Feature extraction noise suppression block FENSB							
	Conv	DConv	BNorm+ReLU	DConv	BNorm+ReLU	DConv	BNorm + ReLu	Conv
Filter size	3	1	\	2	\	1	\	3
Merge	\	\	\	\	\	\	\	Conv

In theory, denoising and deblurring are distinct procedures. Noise tends to appear as a high-frequency component in an image, and denoising removes high-frequency components from images. This leads to defects in most algorithms that use denoising, such as a loss of texture and other details, and the image is blurred after denoising. Deblurring is intended to restore details of the blurred image. Traditional blind deconvolution methods often enhance noise in the image. Therefore, the restoration of images of targets in space involves removing blur and suppressing noise. A special noise suppression module is thus introduced to our proposed network model to improve performance.

### 3.2. Network architecture

The structure of BDATNet is shown in Fig. 1. The entire network features end-to-end mapping. Input images are first processed by the stacked FENSB and asymmetric U-net, respectively, and the image is reconstructed by IRSUBnetwork according to the acquired feature map to obtain the final image. The fusion of the feature map acquired by the FENSB with the input image is used as input to the U-net, which uses the advantages of the FENSB while overcoming its shortcomings. U-net is used as a de-convolution operator for the input map to blindly remove turbulent blur. The IRSUBnetwork is used to reconstruct an image based on a feature map that removes blur and noise. Because the DNSB is added to the convolution process of U-net, its structure is no longer symmetrical: Hence, the new U-net is renamed the Asymmetric U-net. The parameters of each layer in the BDATNet are set as shown in Table 1.

#### 3.2.1. Feature extraction noise suppression block

Based on the characteristics of degradation in the image of the spatial target and deep convolutional neural networks, an FENSB is designed to suppress noise while extracting feature maps. The structure diagram of the FENSB is shown in Fig. 2. It consists of two convolutional layers, three dilated convolutional layers, three normalized layers, and a fusion layer. It is well known that the use of contextual information in the process of reconstructing a degraded image can help obtain a clearer image. Convolutional neural networks usually increase the depth of the network and

size of the filter to obtain a larger receptive field. However, these two methods not only introduce more parameters, but also increase the burden of calculation [64]. Dilated convolution is known for its capacity to expand the receptive field while maintaining the merits of traditional  $3 \times 3$  convolution. A number of studies [39,64–66] have shown that the use of dilated convolution can help balance the size of the receiving field and the depth of the network. Batch normalization is also an important technique for designing neural network models. Ref. [67] has noted that it can achieve fast and stable training, and delivers good denoising performance. In recent years, dilated-convolution and batch normalization have been widely used in the design of denoising neural network models. We use the same strategy to design the FENSB and DNSB. To ensure that the FENSB can extract all image information, the first and last convolutional layers are connected. The parameters of each layer in the FENSB are set as shown in Table 2.

#### 3.2.2. Deblurring noise suppression block and asymmetric U-net

If the feature map acquired by the FENSB is combined with the input image as input to the U-net, the U-net contains noise. Inspired by the FENSB, this paper designs a DNSB to replace the convolutional layer in the process of convolution of U-net. The DNSB contains two convolution layers, a hole convolution layer and a normalization layer. The activation function in DNSB is unified into the ReLU. The structure of the DNSB is shown in Fig. 3, and the parameters of each layer in DNSB were set as shown in Table 3.

To reduce the loss of image information during the de-convolution of U-net, this paper replaces up-sampling in the U-net network with transposed convolution. The first convolutional layer in each DNSB is merged with the corresponding convolutional layer after the transposed convolution. Note that the U-net no longer has a symmetric structure because the DNSB is added during the convolution process. The network structure of Asymmetric U-net and the parameters of each layer are shown in Fig. 4 and Table 4, respectively.

### 4. Network training

An unsupervised learning method was used to pre-train the deep neural network to build a deeper structure. The initialized

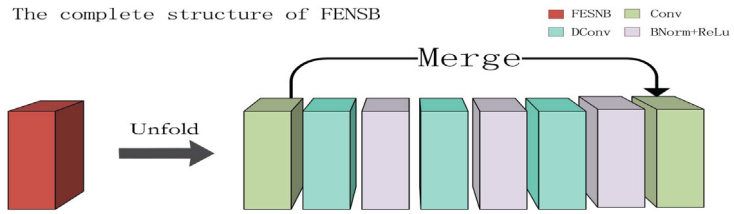


**Fig. 2.** Feature extraction noise suppression block (FENSB) (filter sizes of the 3-layer dilated convolution are  $1 \times 1$ ,  $2 \times 2$  and  $1 \times 1$ .)

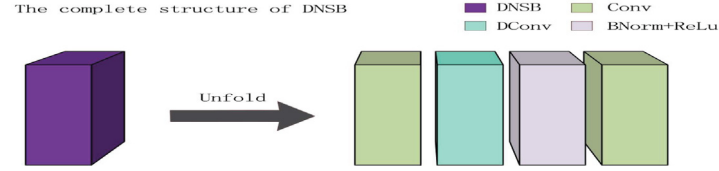


**Fig. 3.** Deblurring noise suppression block (DNSB). The filter size of DConv is  $(1 \times 1)$ .

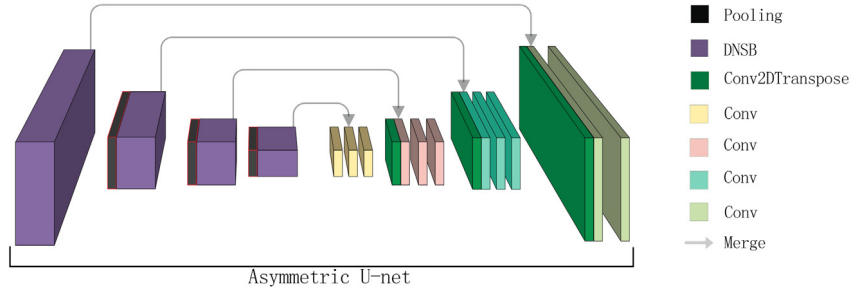


**Fig. 4.** Structure of Asymmetric U-net. (It contains 4 sets of DNSBs and 4 merged layers. The de-convolution process is consistent with U-net. All activation functions are ReLU.)

**Table 3**  
Configurations of the FENSB.

De-blurring noise suppression block (DNSB)			
Layer	Conv	DConv	BNorm+ReLU
Filter size	3	1	3

network weights obtained through unsupervised learning can help improve network stability and avoid the problem of the local minimum. Unsupervised learning is often used to obtain the internal features of related datasets and remove redundant parameters in the input data to obtain low-dimensional features of the given image with a certain robustness.

#### 4.1. Constructing training data

Neural networks for image restoration benefit from a large amount of training data. However, an important problem in restoring images of spatial targets using neural network-based methods is a lack of training data. Because the acquisition of the images of targets in space must require light passing through the atmosphere, the image we can obtain is degraded by turbulence and unclear. It is important to reconstruct such images.

**Table 4**  
Configurations of the Asymmetric U-net.

De-blurring noise suppression block (DNSB)																			
Layer	DNSB	Pool	DNSB	Pool	DNSB	Pool	DNSB	Conv1	Conv1	Conv1	T1	Conv	Conv	Conv	Conv	Conv	Conv	Conv	Conv
1	1	2	2	2	3	3	3	\	3	3	\	3	3	\	3	3	\	3	3
Resize	\	\	\	\	\	\	\	\	\	\	Conv 11	\	\	Conv 9	\	\	Conv 7	\	\

To improve the generalization ability of the trained BDATNet, we carried out the long-exposure atmospheric turbulence degradation processing of images from the Satellite Tool Kit (STK) and the Internet to construct datasets. Our dataset had 400 images (350 from the STK and 50 from the Internet). The classical model of degradation due to atmospheric turbulence was used, as follows [68].

$$h(u, v) = e^{\left\{-3.44\left(\frac{\lambda fU}{r_0}\right)^{5/3}\right\}}, \quad (4)$$

where  $h(u, v)$  is the transfer function of atmospheric turbulence,  $U = \sqrt{(u^2 + v^2)}$  is frequency,  $\lambda$  is wavelength, and  $f$  is the focus of the optical system. On the spatial scale, the disturbance in the wavefront due to atmospheric turbulence was usually characterized by the atmospheric dry length  $r_0$ , which is a characteristic measure that reflects the intensity of atmospheric turbulence. Gaussian noise and Poisson were added to the simulated image, and the parameter  $\sigma$  of Gaussian noise was determined as follows:

$$\sigma = e \times \frac{\|I\|}{\sqrt{M \times N}}, \quad (5)$$

where  $e$  is the percentage of error. The larger the value of  $e$  is, the heavier is noise.  $\|\cdot\|$  is the Frobenius norm of the matrix,  $I$

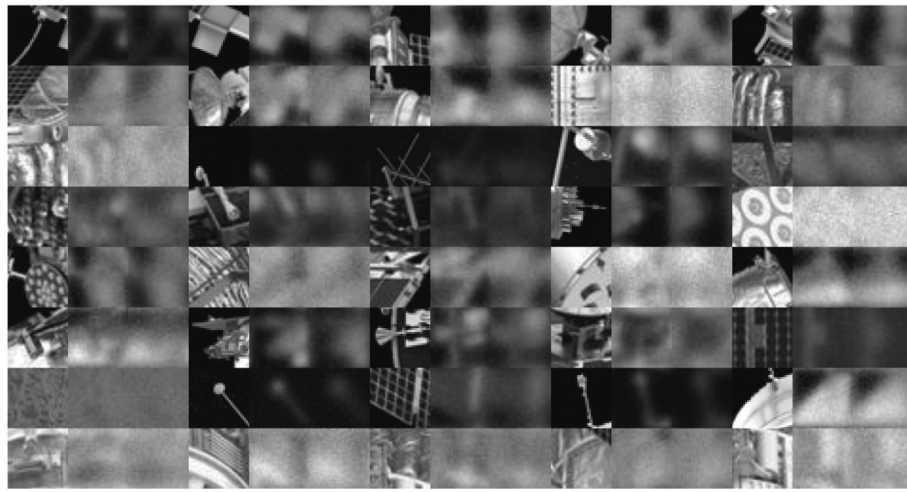


**Fig. 5.** Training dataset constructed by the atmospheric turbulence degradation function, (Eq. (4)).

**Table 5**

The parameters of deblurring and noise levels of three types of simulation test images.

	Mildly degraded	Moderately degraded	Highly degraded
$r_0$	0.005	0.01	0.02
$e$	0.05	0.05	0.05
$\lambda$	5	5	5

represents an image, and  $M$  and  $N$  are the width and height of  $I$ , respectively.

When constructing data for the simulated degradation due to atmospheric turbulence, we enhanced 400 original images to obtain 1600 images (first rotated 90 degrees clockwise and then scaled by a multiple of 0.6). We then used Eq. (4) to perform long-exposure turbulence degradation processing on the 1600 images to obtain a dataset containing 6400 degraded images. To better fit the process of turbulence degradation, we used four blur parameters  $r_0$ , and added Gaussian and Poisson noises. Finally, we cut the 6400 degraded images at intervals of 25 pixels to obtain 252,928 image blocks with a size of  $32 \times 32$  for network training. Note that during the cropping process, we discarded small images with more than 95% of a black background. Some of the training data constructed in this paper are shown in Fig. 5. The test dataset was completely selected from the simulated images excluded from the training dataset, as shown in Fig. 6. The parameter settings for the three degrees of degradation are shown in Table 5, and the data from the original image are shown in Fig. 7, where (a), (b), (c), and (d) show the images captured on the International Space Station (ISS) at different times and angles. It is clear from Fig. 7 that the real image was subject to significant interference due to noise in addition to the blur due to atmospheric turbulence. We used histogram statistics to compare the simulated data with the corresponding empirical data, as shown in Fig. 8. It is clear that our simulation and empirical data had similar gray information distributions, which shows that the former can be used as an alternative to the latter to evaluate the performance of the algorithm.

#### 4.2. Step-by-step training process

A highly degraded image is extremely difficult to recover and cause to converge during network training. According to the degree of blur and level of noise, the training set used to pre-training was divided in a series from easy to difficult, represented by  $T_1, T_2, \dots, T_n$ , forming the complete dataset  $T$  for the final

training network. During the training process, training set  $T_i$  was used to obtain the weights of stage  $T_i$ . Based on the weights, the more difficult training set  $T_{i+1}$  was then used to train the network, followed by training set  $T_{i+2}, \dots$ , and, finally, the most difficult dataset  $T_n$  was used to train the network. After all  $T_i$  level stages of training had been completed, the comprehensive data training set  $T$  was used for to train the entire network. Parameters of the data for pre-training and final training are shown in Table 6. Experiments showed that the proposed method made the network easier to train and converge than methods trained on all data at once. Moreover, many experiments show that this method is robust and insensitive to process noise, and obtained stable results of convergence each time. The step-by-step training process is shown in Algorithm 1.

#### Algorithm 1 Iterative training scheme.

---

**Require:**  
The dataset  $\{T_1, T_2, \dots, T_n\}$  for pre-training and the dataset  $T$  for final training; the weights of initialization of network  $W_0^P$ .

**Ensure:**  
Network weights  $W$ .

```

1: for  $i \leftarrow 1$  to  $n$  do
2:   Initialize the weight  $W_0^b \leftarrow W_{i-1}^P$ ;
3:   for  $j \leftarrow 1$  to  $t$  do
4:     Pre-training the network using batches in  $T_i$  ;
5:     Updating network weights  $W_j^b \leftarrow W_{j-1}^b$ ;
6:   end for
7:   Updating weights of network  $W_i^P \leftarrow W_t^b$ ;
8: end for
9: Initialize weights of the finally trained network  $W_0^l \leftarrow W_n^P$ ;
10: for  $i \leftarrow 1$  to  $k$  do
11:   Training the full network using batches in  $T$ ;
12:   Updating weights of network  $W_j^l \leftarrow W_{j-1}^l$ ;
13: end for
14: Weights of the final network  $W \leftarrow W_k^l$ ;

```

---

In the experiment, images of size  $32 \times 32$  were used for network training. For testing, the weight of the entire network was migrated to images of different sizes, and the convolutional network could perform deblurring only by changing the image size at the input. The results of the numerical experiment show that the network achieved the best convergence when the learning rate was  $1e-5$  and batch size was 64 in network pre-training and formal training. Moreover, when the numbers of iterations for pre-training and formal training were greater than 200 and 150, respectively, significant over-fitting occurred. Therefore, the number of iterations of pre-training and formal training were set to 200 and 150, respectively.

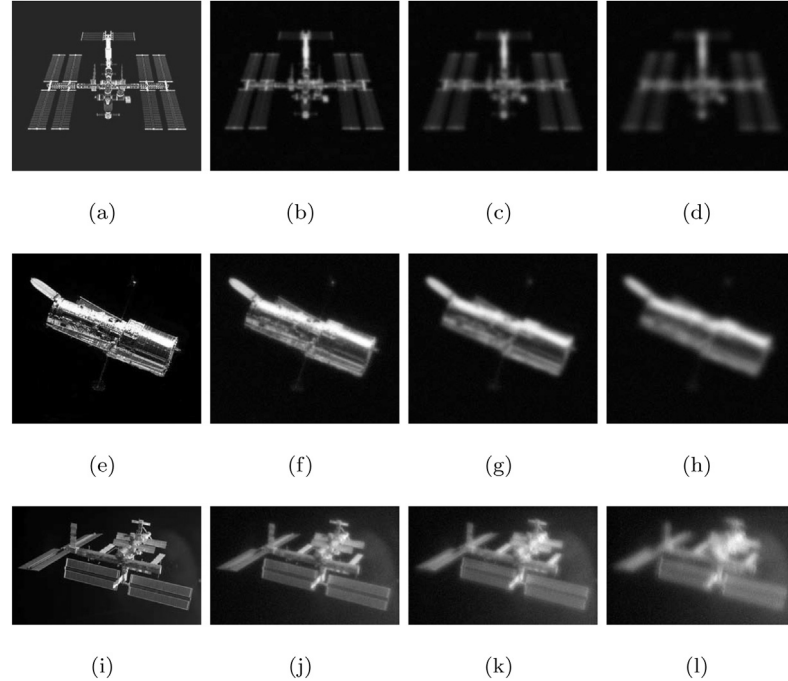


**Fig. 6.** Simulation test images. ((a) and (i) show the original ISS images. (e) is the original image of the Hubble telescope. (b), (f), and (j) are mildly degraded images. (c), (g), and (k) are moderately degraded images. (d), (h), and (l) are highly degraded images.)

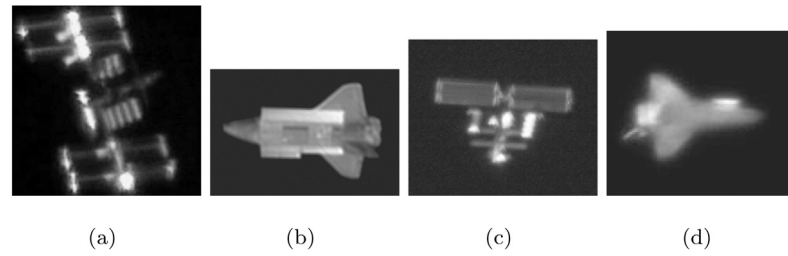


**Fig. 7.** Real test images.

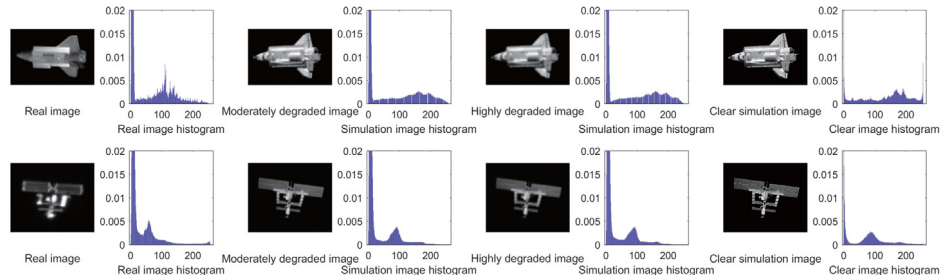


**Fig. 8.** Histogram statistical analysis of empirical degradation data and simulation test data.

**Table 6**  
Degrees of blur and noise levels of different datasets.

Dataset	Pre-training				Formal training
	$T_1$	$T_2$	$T_3$	$T_4$	
Dataset size	63232	126464	189696	252928	252928
$r_0$	0.005	0.005	0.005	0.005	0.005
		0.01	0.01	0.015	0.01
		0.015	0.017	0.015	0.02
e	0.05	0.05	0.05	0.03	0.05
$\lambda$	5	5	5	3	5
Iterations	200	200	200	200	150

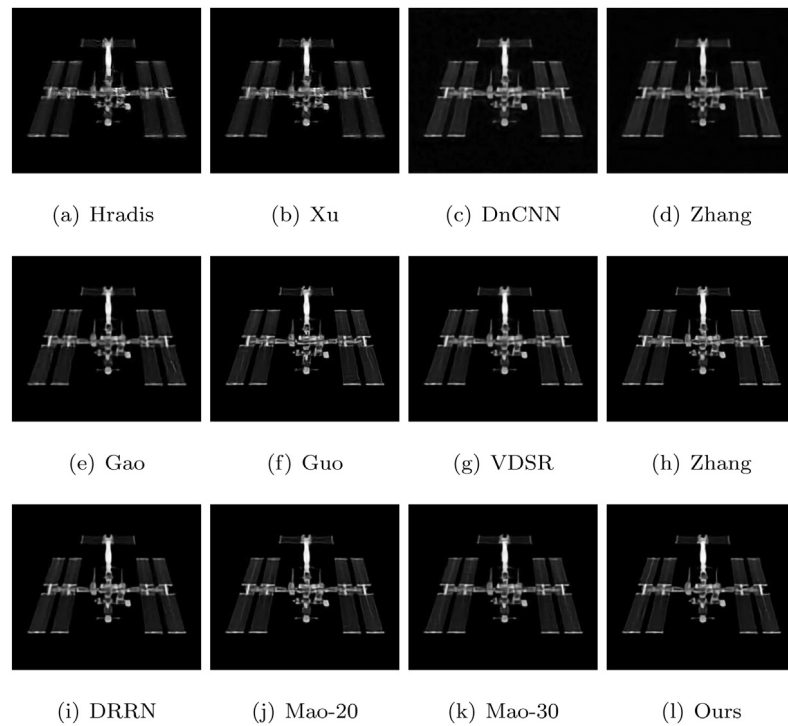


**Fig. 9.** The restored images of the moderate turbulence-degraded images of ISS (Fig. 6(c)).

## 5. Comparative analysis of experiments

The reference image evaluation index (using the clear image as the reference image) can effectively evaluate the effect of image restoration. However, for the restoration of space target images with more high image degradation, no effective objective evaluation indexes can be used [24]. The simulated image was objectively evaluated by the reference image evaluation index, while the real image was subjectively evaluated by human visual observation. The reference image evaluation indexes used in this paper are: SNR, peak SNR (PSNR), mean square error (MSE), average absolute difference (AAD) and image fidelity (IF). The detailed definitions of these objective indexes were in [46]. In order to better analyze the performance of the algorithm, we have selected several representative deep learning methods for comparative experimental analysis. In literature [46], a lot of analyses done on the traditional methods of spatial target image restoration shows that their effect was not satisfactory. Therefore, this article no longer compares and analyzes with traditional methods. In recent years, learning-based especially deep learning based methods for single-frame image have achieved good results, such as Zhang [29], Guo [32], VDSR [39], DRRN [40], Gao [46], Xu [57], Hradis [58], Mao [60] (Mao-20 and Mao-30 represent the network depths are 20 and 30, respectively), DnCNN [67] and Zhang [69].

### 5.1. Experimental analysis of simulation images

The comparison results of various restoration methods for the moderate turbulence-degraded ISS image (Fig. 6(c)) with reference evaluation indicators are shown in Table 7. As can be seen from Table 7, the proposed method was the best among all the compared methods on the PSNR evaluation index. The second-ranked Mao-30 and the third-ranked Mao-20 also achieved relatively competitive results, but there was still a gap with our approach. In particular, the PSNR of our method is improved by more than 0.3% compared to the second-ranked Mao-30. The restoration results of the moderate turbulence-degraded ISS image (Fig. 6(c)) are shown in Fig. 9. It can be seen that there

**Table 7**  
The objective assessment of state-of-the-art methods for Fig. 6(c).

	AAD	SNR	PSNR	IF	MSE
Hradis [58]	0.0189	7.6554	24.4692	47.8438	0.0035
Xu [57]	0.0187	7.7371	24.5509	47.8470	0.0035
DnCNN [67]	0.0178	7.9022	24.7160	47.8533	0.0033
Zhang [69]	0.0170	7.9566	24.7704	47.8553	0.0033
Gao [46]	0.0165	8.5099	25.3237	47.8745	0.0029
Guo [32]	0.0154	8.6720	25.4858	47.8796	0.0028
VDSR [39]	0.0157	9.1130	25.9268	47.8927	0.0025
Zhang [29]	0.0157	9.1488	25.9627	47.8937	0.0025
DRRN [40]	0.0151	9.2494	26.0632	47.8965	0.0024
Mao-20 [60]	0.0150	9.3349	26.0704	47.8988	0.0024
Mao-30 [60]	0.0147	9.3857	26.1213	47.9001	0.0023
Ours	<b>0.0146</b>	<b>9.4172</b>	<b>26.1998</b>	<b>47.9002</b>	<b>0.0022</b>

was obvious turbulence in the restoration image obtained by the Hradis algorithm (Fig. 9(a)), and the visual effects of the restored images obtained by the Xu, DnCNN and Zhang algorithms were basically the same, with slight ambiguity (Figs. 9(a), 9(b), 9(c), respectively). The rest of the methods had relatively good visual effects and Fig. 9(l) had better continuous consistency.

Table 8 is a comparison of the reference evaluations of the various restoration methods for the ISS highly degraded image (Fig. 6(d)). The influencing factors of highly degraded images are more complicated, so the restoration of degraded image is more difficult. In general, the restoration results of highly degraded images are significantly worse than those of moderately degraded images. It can be seen from Fig. 6(d) that the degraded image lost most of the information, leaving only the overall blurred outline. From the evaluation index, the recovery results of all algorithms for moderate turbulence-degraded images are significantly better than those for severe turbulence-degraded images. And for methods of severe turbulence-degraded image restoration, our method is significantly better than other methods. Particularly, the PSNR of our method was 24.0207, which was higher than the second-ranked algorithm DRRN by more than 1.38%. The third-ranked method is the VDSR. As can be seen from Figs. 6(c)

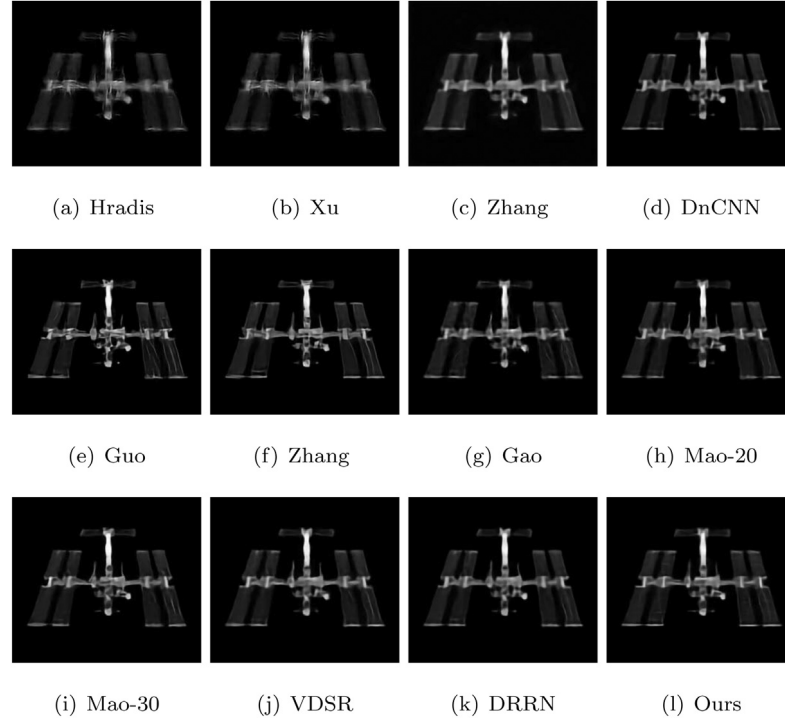


**Fig. 10.** The restored images of the severe turbulence-degraded images of ISS (Fig. 6(d)).

and 6(d), methods proposed by Mao were relatively good for the restoration of moderate turbulence-degraded images, but the restoration results for severe turbulence-degraded images were relatively poor. Noticed that the results of Mao-30 and Mao-20 were relatively close, and increasing the depth of the network does not bring about the desired results. The DRRN and Gao methods had improved by two rankings respectively, and the VDSR method had improved by three rankings, indicating that the three methods are better than some methods in the restoration of severe turbulence-degraded images. The rankings of Hradis and Xu had not changed, and they were still the worst, indicating that these methods are not ideal for the restoration of atmospheric turbulence-degraded images. The restoration results of the severe turbulence-degraded ISS image (Fig. 6(d)) are shown in Fig. 10. As can be seen, the visual effect of restoration images obtained by Hradis, Xu and Zhang algorithms were basically the same, with obvious blur (Figs. 10(a), 10(b), and 10(c), respectively). The quality of restoration images obtained by the Guo, Zhang and Gao algorithms were relatively consistent, with significant distortion and confusing texture information. The quality of restoration images obtained by DRRN and Ours were similar, but Ours had better continuous consistency and richer texture information (Figs. 10(k) and 10(l)).

The comparison results of various restoration methods for the moderate degraded Hubble telescope image (Fig. 6(g)) with reference evaluation indicators are shown in Table 9. Restoring degraded images from the Hubble telescope is more difficult because the surfaces of these images have a more complex texture. In the restoration effect of each algorithm on the Hubble telescope image and the ISS degraded image, the Mao-30 method had dropped three rankings on the index, and the ranking was behind the Mao-20. This was inconsistent with the conclusion in the literature [60] that the deeper the network recovery effect will be better. Xu's method was still not ideal, and the results of the Hradis method were significantly improved. Our method was obviously superior to the other methods in terms of evaluation indicators, indicating that the network proposed has strong

**Table 8**  
The objective assessment of state-of-the-art methods for Fig. 6(d).

	AAD	SNR	PSNR	IF	MSE
Hradis [58]	0.0253	5.5883	22.4021	47.7392	0.0057
Xu [57]	0.0252	5.6534	22.4672	47.7433	0.0056
Zhang [69]	0.0224	6.1051	22.9189	47.7702	0.0051
DnCNN [67]	0.0218	6.2690	23.0828	47.7793	0.0049
Guo [32]	0.0214	6.2920	23.1058	47.7805	0.0048
Zhang [29]	0.0209	6.5264	23.3402	47.7929	0.0046
Gao [46]	0.0214	6.5460	23.3598	47.7939	0.0046
Mao-20 [60]	0.0199	6.7943	23.6081	47.8062	0.0043
Mao-30 [60]	0.0201	6.8487	23.6625	47.8088	0.0043
VDSR [39]	0.0207	6.8492	23.6630	47.8088	0.0043
DRRN [40]	0.0200	6.8807	23.6945	47.8103	0.0042
Ours	<b>0.0195</b>	<b>7.2069</b>	<b>24.0207</b>	<b>47.8251</b>	<b>0.0039</b>

**Table 9**  
The objective assessment of state-of-the-art methods for Fig. 6(g).

	AAD	SNR	PSNR	IF	MSE
Xu [57]	0.0296	11.6895	24.6563	17.2012	0.0034
DnCNN [67]	0.0285	12.2144	24.8673	17.5312	0.0034
Zhang [69]	0.0232	12.4883	24.9413	17.5348	0.0032
Hradis [58]	0.0207	12.7711	25.0186	17.5369	0.0031
Guo [32]	0.0197	12.8879	25.3408	17.5398	0.0029
Gao [46]	0.0193	12.9322	25.3852	17.5403	0.0028
Zhang [29]	0.0191	13.0679	25.5208	17.5419	0.0028
Mao-30 [60]	0.0189	13.3937	25.8466	17.5454	0.0026
VDSR [39]	0.0187	13.3987	25.8517	17.5455	0.0025
DRRN [40]	0.0186	13.4596	25.9126	17.5461	0.0025
Mao-20 [60]	0.0186	13.4911	25.9441	17.5465	0.0025
Ours	<b>0.0184</b>	<b>13.5409</b>	<b>25.9938</b>	<b>17.5670</b>	<b>0.0024</b>

feature learning ability. The restoration effect of the Hubble telescope's moderate turbulence-degraded image (Fig. 6(g)) is shown in Fig. 11. From the visual effect, the restored image obtained by the Xu method had obvious blur and the image texture was seriously lost (Fig. 11(a)). The DnCNN method had a slight artifact around the restored image (Fig. 11(b)). The visual effects of the restored images obtained by the other methods were close to

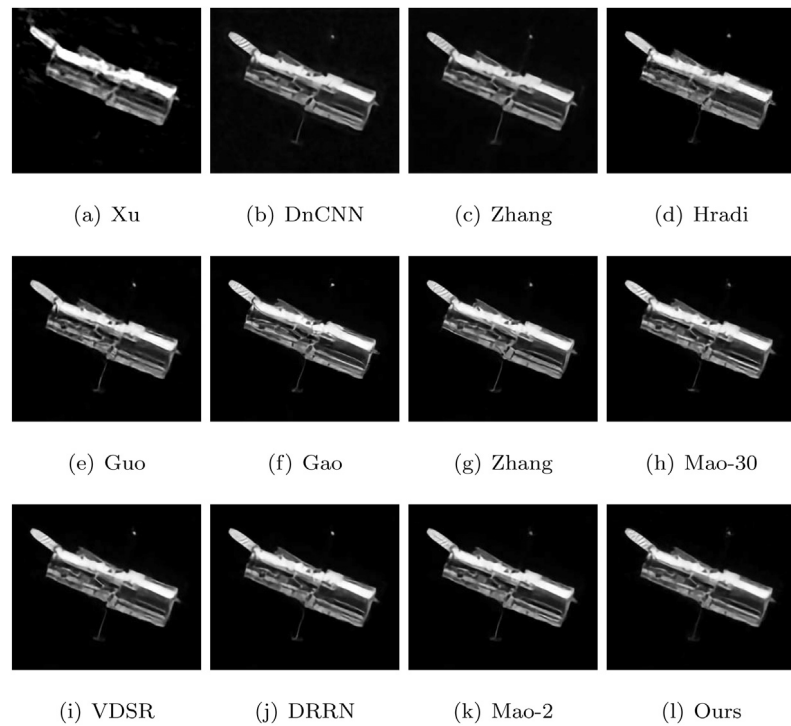


**Fig. 11.** The restored images of the moderate turbulence-degraded images of Hubble telescope (Fig. 6(g)).

**Table 10**

The objective assessment of state-of-the-art methods for Fig. 6(h).

	AAD	SNR	PSNR	IF	MSE
Xu [57]	0.0292	10.1685	22.1562	17.1935	0.0052
DnCNN [67]	0.0242	10.8729	23.3259	17.5094	0.0046
Zhang [69]	0.0245	10.9710	23.4240	17.5113	0.0045
Guo [32]	0.0239	11.2509	23.7039	17.5162	0.0042
Hradis [58]	0.0239	11.2821	23.7580	17.5143	0.0041
Zhang [29]	0.0233	11.4738	23.9268	17.5200	0.0040
Gao [46]	0.0233	11.6040	24.0569	17.5221	0.0039
VDSR [39]	0.0227	11.6452	24.0982	17.5228	0.0038
Mao-30 [60]	0.0227	11.6983	24.1513	17.5236	0.0038
Mao-20 [60]	0.0226	11.7002	24.1532	17.5236	0.0037
DRRN [40]	0.0226	11.8080	24.2009	17.5206	0.0037
Ours	<b>0.0225</b>	<b>11.8561</b>	<b>24.3091</b>	<b>17.5260</b>	<b>0.0036</b>

**Table 11**

The objective assessment of state-of-the-art methods for Fig. 6(k).

	AAD	SNR	PSNR	IF	MSE
DnCNN [67]	0.0455	10.7581	24.3716	22.8959	0.0036
Zhang [69]	0.0399	11.6838	25.2972	22.9120	0.0029
Xu [57]	0.0281	12.4118	26.0253	22.9225	0.0024
VDSR [39]	0.0272	12.4790	26.0925	22.9234	0.0024
Hradis [58]	0.0219	13.2100	26.8235	22.9321	0.0020
Gao [46]	0.0206	13.4549	27.0684	22.9347	0.0019
Guo [32]	0.0205	13.4960	27.1095	22.9351	0.0019
Zhang [29]	0.0205	13.5915	27.2050	22.9361	0.0019
DRRN [40]	0.0204	13.6281	27.2416	22.9365	0.0018
Mao-30 [60]	0.0203	13.8739	27.4873	22.9389	0.0017
Mao-20 [60]	0.0201	14.1846	27.7981	22.9417	0.0016
Ours	<b>0.0192</b>	<b>14.3568</b>	<b>27.9703</b>	<b>22.9432</b>	<b>0.0015</b>

each other and cannot be directly distinguished by the naked eye.

The comparison results of various restoration methods for the severe degraded Hubble telescope image (Fig. 6(h)) with reference evaluation indicators are shown in Table 10. From the evaluation indicators, the recovery results of our method were better than the other methods. Moreover, the PSNR evalua-

tion index was higher than the second-ranked DRRN by 0.45%. The rankings of Gao and DRRN methods had increased. The results of the Xu method were ranked lower and the recovery result was still poor. It is noted that Mao-20 and Mao-30 have little difference in the restoration results of severe turbulence-degraded images of ISS and Hubble telescope, which reflects that it is impossible to obtain expected restoration only by increasing the depth of the network. By investigating the restoration of two severely degraded images, the Gao and DRRN methods can achieve better results than the general methods on heavily degraded images. The restoration effect of the Hubble telescope's severe turbulence-degraded image (Fig. 6(h)) is shown in Fig. 12. From the visual effect, the restored images obtained by the Xu method had a poor recovery result (Fig. 12(a)), which had obvious blur and serious image information loss. The restored images obtained by the DnCNN and Zhang methods had similar visual effects, and there were significant artifacts around the image (Figs. 12(b), 12(c)). The restored image obtained by the Guo method had the strongest visual impact (Fig. 12(d)). However, it was significantly different from Fig. 6(e)(the original image), which had changed the texture information of the image. The visual effects of the restored map obtained by the other methods were basically the same.

The comparison results of various restoration methods for the moderate turbulence-degraded ISS image (Fig. 6(k)) with reference evaluation indicators are shown in Table 11. As can be seen from Table 11, the proposed method was the best among all the compared methods on all evaluation indexes. Particularly, compared with the second-ranked Mao-20, The PSNR evaluation index of our method was about 0.62% higher. From the comprehensive analysis of the evaluation indicators in Tables 7–10, we can see that (1) The restoration effect ranking of the Xu and Hradis methods were significantly increased, and the ranking of the VDSR method was significantly reduced, indicating all the three methods had relatively poor stability to the restoration of atmospheric turbulence-degraded images. (2) The rankings of DnCNN and Zhang had declined, but the decline was not

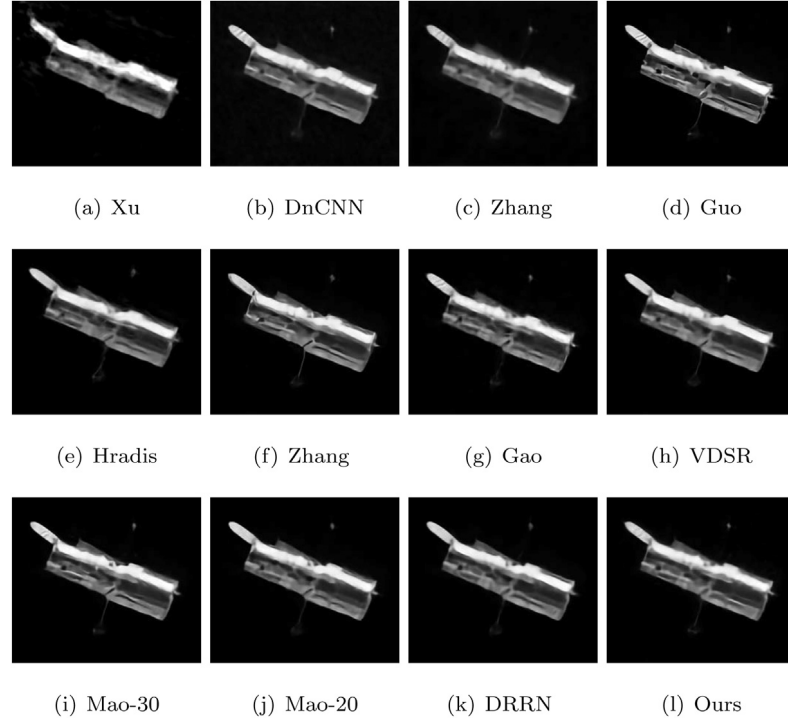


**Fig. 12.** The restored images of the severe turbulence-degraded images of Hubble telescope (Fig. 6(h)).

large, which shows that the ability of these two methods to recover from atmospheric turbulence-degraded images is relatively poor. (3) The three methods (Our, Mao and DRRN) were relatively stable, and the restoration of the target image of the degraded space was relatively good. The restoration images of different algorithms for the moderate turbulence-degraded ISS image (Fig. 6(k)) are shown in Fig. 13. From the visual effect, the recovery results of all methods were basically the same, and it is impossible to visually analyze the advantages and disadvantages of various algorithms from the naked eye. This may be due to the obvious texture information in Fig. 6(k).

The comparison results of various restoration methods for the severe degraded ISS image (Fig. 6(l)) with reference evaluation indicators are shown in Table 12. As can be seen from Table 12, from all evaluation indexes, the results of our method were the best, and the PSNR evaluation index was about 1.5% higher than the second-ranked Mao-20. The ranking of Gao methods had been greatly improved, while the rankings of DRRN and VDSR methods were still relatively poor. The restoration results of all degraded images show that increasing the depth of the network in the Mao-20 and Mao-30 methods does not achieve the expected results, while the Gao method can achieve better results than the general methods on heavily degraded images. Therefore, the Gao method has room for improvement. The restoration effect of the ISS image (Fig. 6(l)) for severe turbulence degradation is shown in Fig. 14. From the visual point of view, the visual effects of the four methods of DnCNN, Zhang, VDSR and DRRN were relatively good and basically the same (Figs. 14(a), 14(b), 14(f), 14(g), respectively). Although these four methods had a better visual effect, the restored image was too smooth and more image texture information was lost. Although the restoration of our method (Fig. 14(i)) was not as visual as the above four methods, the restored image was more realistic and had more texture and is superior to other methods.

## 5.2. Experimental analysis of real data

The restoration results of the moderately and highly degraded real images (in Fig. 7) are shown in Figs. 15–18. Among them,

**Table 12**  
The objective assessment of state-of-the-art methods for Fig. 6(l).

	AAD	SNR	PSNR	IF	MSE
DnCNN [67]	0.0528	9.2649	22.8784	22.8614	0.0051
Zhang [69]	0.0474	9.5443	23.1578	22.8688	0.0048
Hradis [58]	0.0384	9.9447	23.5582	22.8786	0.0044
Xu [57]	0.0395	10.3145	23.9280	22.8868	0.0040
Zhang [29]	0.0320	10.5540	24.1674	22.8918	0.0038
VDSR [39]	0.0337	10.6156	24.2291	22.8931	0.0037
DRRN [40]	0.0341	10.6247	24.2382	22.8933	0.0037
Gao [32]	0.0265	10.8238	24.4373	22.8971	0.0036
Mao-30 [60]	0.0260	11.6112	25.2247	22.9109	0.0030
Gao [46]	0.0259	11.6160	25.2295	22.9109	0.0029
Mao-20 [60]	0.0246	11.7271	25.3405	22.9127	0.0029
Ours	<b>0.0241</b>	<b>12.0975</b>	<b>25.7110</b>	<b>22.9182</b>	<b>0.0026</b>

Figs. 15 and 16 are the restoration results of the moderately degraded real images (Figs. 7(a) and 7(b)), and Figs. 17 and 18 are the restoration results of the highly degraded real images (Figs. 7(c) and 7(d)). As mentioned earlier, the literature [24] analysis shows that there is no reliable objective evaluation index for de-blurring image. Moreover, we found it more difficult to objectively evaluate the restoration of the highly degraded space target images. From the restoration results of all real degraded images, the restored image of the DnCNN method had poor visual effects and relatively obvious noise and artifacts. The image restored by our method had better continuous consistency, the image structure features were more obvious, and the visual effect was better.

In order to more intuitively and objectively compare the effectiveness of various restoration methods on the restoration of real test images, we performed a histogram statistical analysis on the restored images of real test images, and the results are shown in Figs. 19–22. All methods have significantly improved image quality. Especially Mao, Gao and our method, the histogram distribution of the restored image is ideal. Moreover, as can be seen from Figs. 18 and 21, the advantages of our method are more obvious.

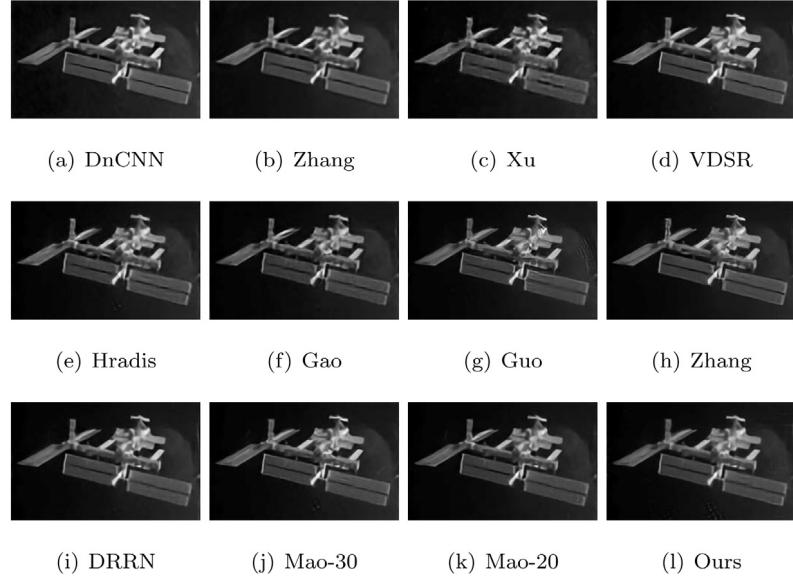


**Fig. 13.** The restored images of the moderate turbulence-degraded images of ISS (Fig. 6(k)).

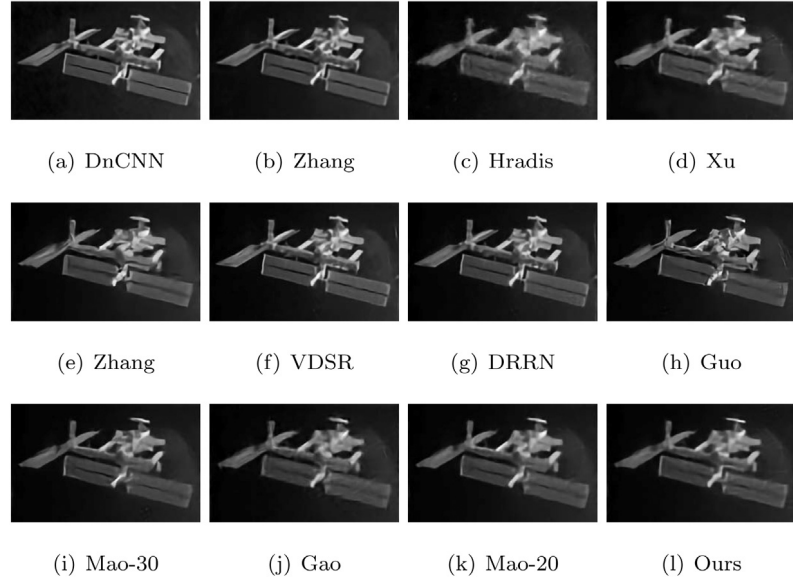


**Fig. 14.** The restored images of the severe turbulence-degraded images of ISS (Fig. 6(l)).

The comprehensive experimental results show that: (1) DnCNN and Zhang [69] can better recover the degraded images with mild blur and mild noise. However, they are sensitive to noise and blur, and it is difficult to obtain expected restoration for images with severely blurred or multiple noise coupling degradation. (2) DRRN is originally used for image super-resolution. From the comprehensive analysis of the evaluation indicators, the recovery result of this method is relatively good, and it is a method with more room for improvement. (3) The restoration results of the Mao-20 and Mao-30 methods on the severely degraded images of atmospheric turbulence are basically the same, indicating that the increase of network depth alone cannot achieve a good expected effect. Therefore, the ideas described in [60] are not applicable to spatial target image restoration of atmospheric turbulence degradation. (4) The Gao method has a certain effect on the restoration of severely degraded images, which deserves further research and improvement. (5) From the comprehensive analysis of the visual effects of multiple indicators

and restored images, the proposed method is the best of all comparison methods. The advantage is even more pronounced in the case of severe degradation. In particular, the average PSNR index increased by about 1.4%, indicating that our method restored the degraded image with less edge oscillation effect and better visual pleasure.

## 6. Conclusions

End-to-end neural network models have recently been designed for simultaneous denoising and deblurring. Although both denoising and deblurring are part of image reconstruction, they are very different in principle. An image of the spatial target is often affected by blur due to turbulence and multiple types of noise, which makes restoring it more difficult. In view of this, we proposed and tested a neural network model for the

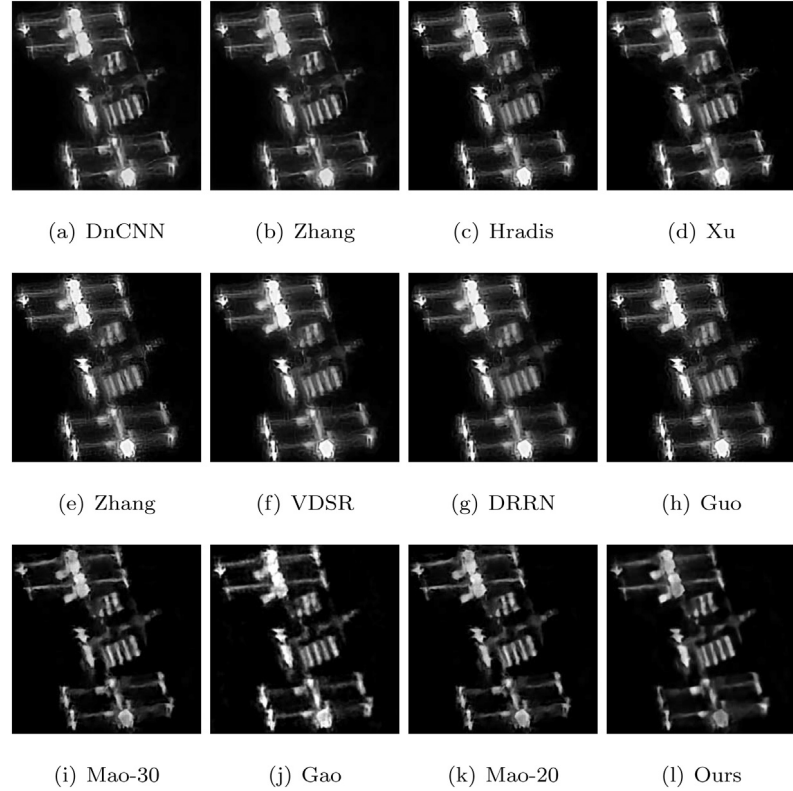


**Fig. 15.** The restoration results of real moderate turbulence-degraded image (Fig. 7(a)).

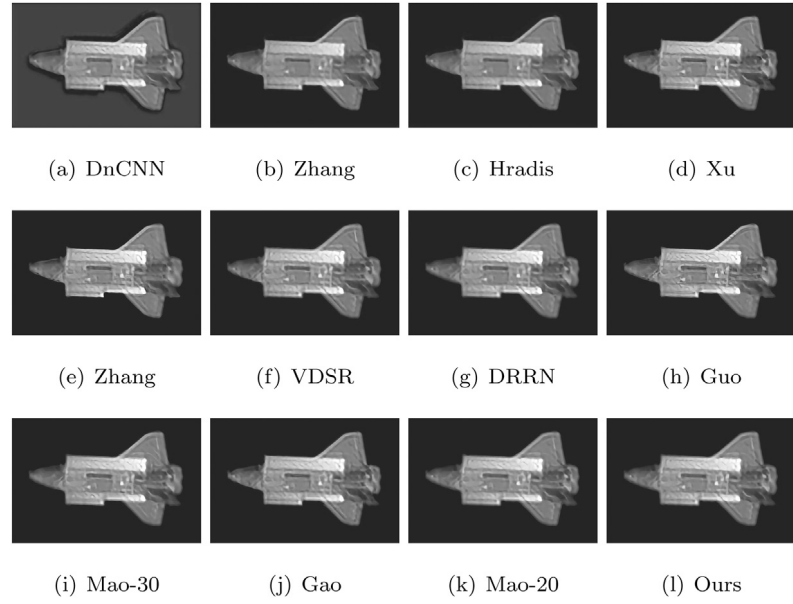


**Fig. 16.** The restoration results of real moderate turbulence-degraded image (Fig. 7(b)).

blind restoration of degraded images of spatial targets. The main characteristics of the proposed network model are the design of the modules FENSB and DNSB with significant noise suppression capabilities. Images are restored through skip connection based on suppressing noise to obtain clear, restored images.

During model training, a simulation training dataset was first constructed based on a three-dimensional model of the spatial target and the model of the image subjected to atmospheric

turbulence. Histogram information showed that the simulation data had a distribution similar to that of the empirically obtained degraded image. For the problem whereby it is difficult to directly train the neural network on severely degraded images, we used a step-by-step training method. The results of experiments on the simulated and empirical data show that the proposed method outperformed other methods. We also found that the more severe

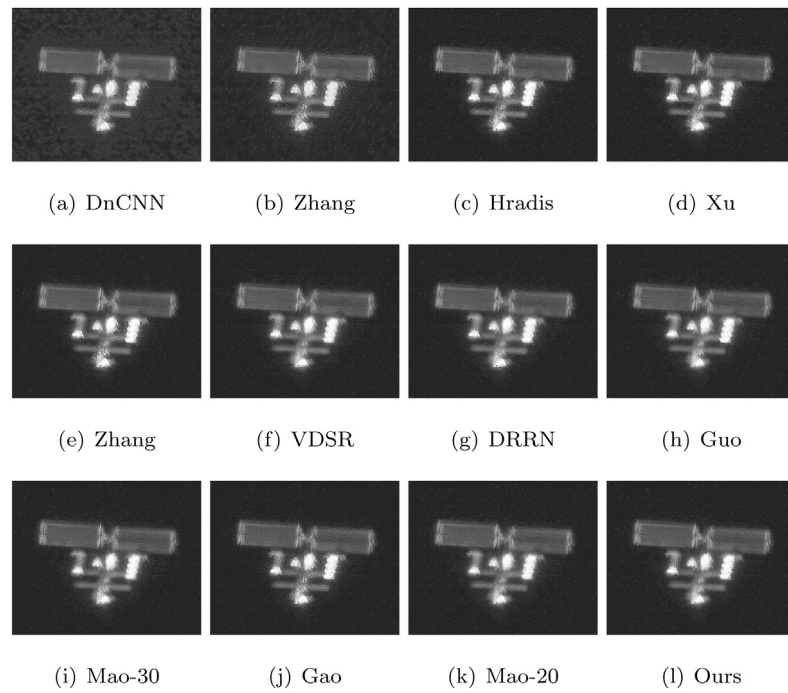


**Fig. 17.** The restoration results of real severe turbulence-degraded image (Fig. 7(c)).

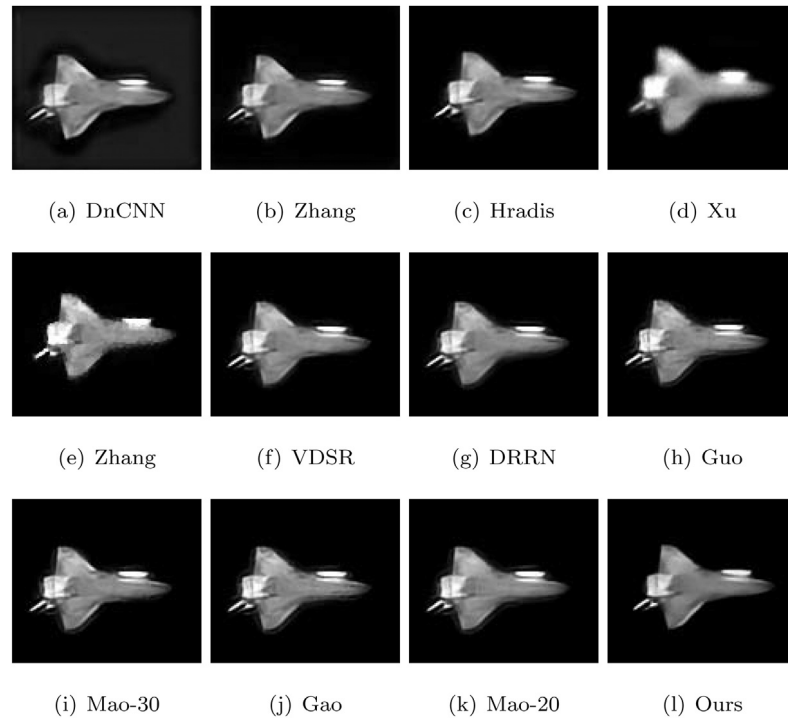


**Fig. 18.** The restoration results of real severe turbulence-degraded image (Fig. 7(d)).

the degradation of the image was, the more competitive our method was.

Ground-based images of spatial targets are significantly affected by environmental conditions and distances to the targets. There are three directions that should be considered in research in the future: (1) using prior knowledge to design a neural network model more suitable for the degradation and restoration of turbulence-blurred images; (2) using deep neural networks to restore multi-frame turbulence-blurred images; and (3) combining the characteristics of optical imaging in turbulent environments

with the latest results, such as the algorithm in reference [49], for further research and exploration.

#### Declaration of competing interest

No author associated with this paper has disclosed any potential or pertinent conflicts which may be perceived to have impending conflict with this work. For full disclosure statements refer to <https://doi.org/10.1016/j.asoc.2020.106131>.

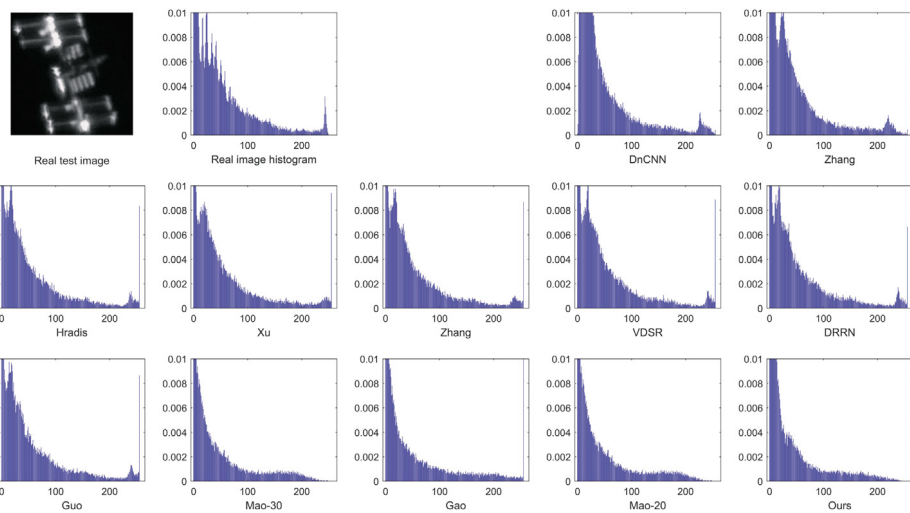


**Fig. 19.** Histogram statistical analysis of real degradation data (Fig. 7(a)).

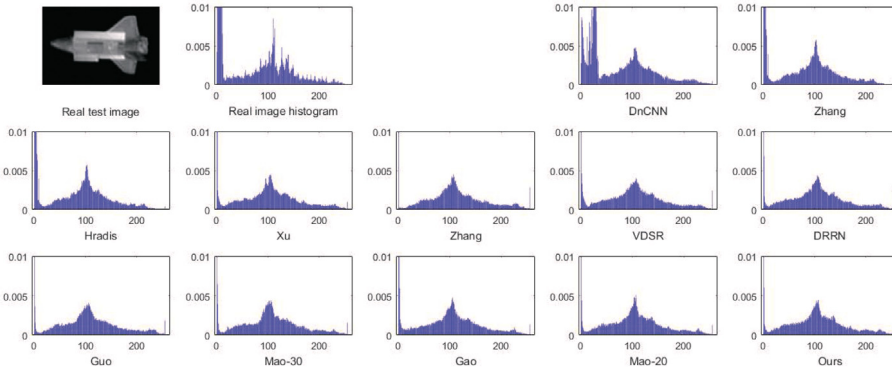


**Fig. 20.** Histogram statistical analysis of real degradation data (Fig. 7(b)).

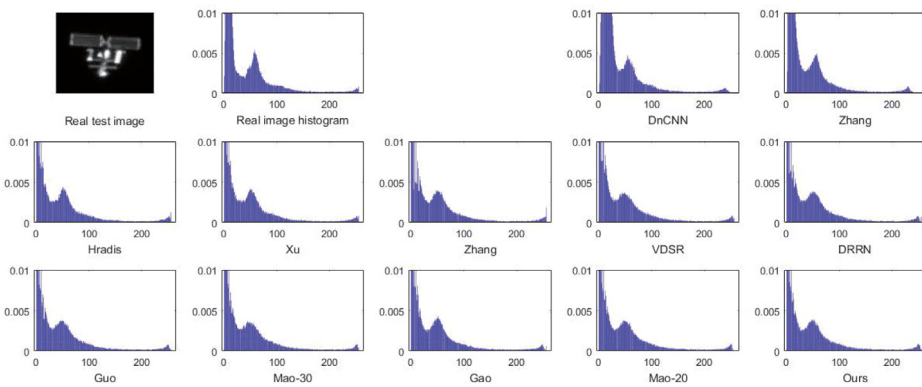


**Fig. 21.** Histogram statistical analysis of real degradation data (Fig. 7(c)).

## CRediT authorship contribution statement

**Gongping Chen:** Data curation, Software, Writing - original draft. **Zhisheng Gao:** Conceptualization, Methodology, Supervision, Writing - reviewing & editing, Validation. **Qiaolu Wang:** Visualization, Investigation. **Qingqing Luo:** Software, Validation.

## Acknowledgments

This work has been partially supported by the Ministry of education Chunhui project, China (Grant No: Z2016149), the Key scientific research fund of Xihua University, China (Grant No: Z17134), Xihua University Key Laboratory Development Program

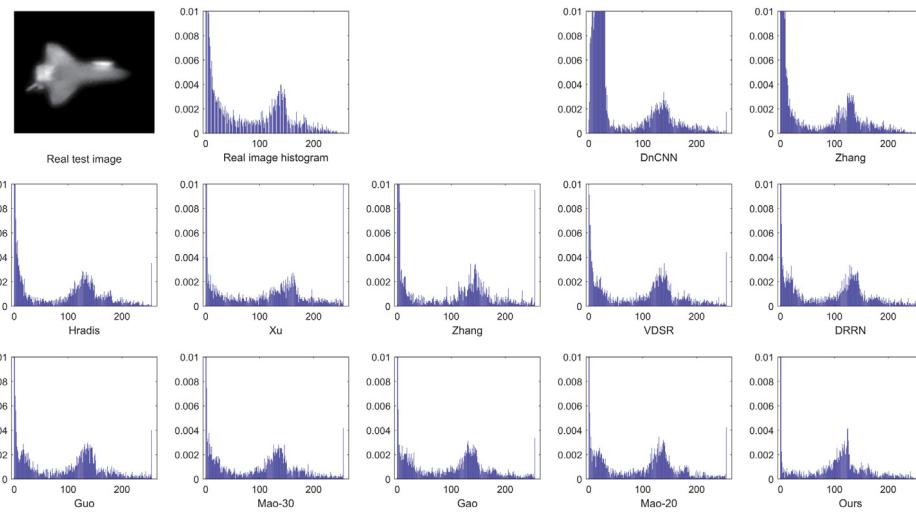


**Fig. 22.** Histogram statistical analysis of real degradation data (Fig. 7(d)).

(Grant No: szjj2017-065), Xihua University Graduate Innovation Fund Research Project (Grant No: ycjj2018067, ycjj2018044) and Sichuan science and technology program, China (Grant No: 2019YFG0108).

## References

- [1] D. Li, R.M. Mersereau, S. Simske, Atmospheric turbulence-degraded image restoration using principal components analysis, *IEEE Geosci. Remote Sens. Lett.* 4 (2007) 340–344.
- [2] W.E.K. Middleton, *Vision Through the Atmosphere*, University of Toronto Press, Toronto, Canada, 1952.
- [3] M.C. Roggemann, B.M. Welsh, B.R. Hunt, *Imaging Through Turbulence*, CRC press, 2018.
- [4] M. Shimizu, S. Yoshimura, M. Tanaka, et al., Super-resolution from image sequence under influence of hot-air optical turbulence, in: IEEE International Conference on Computer Vision, ICCV, 2008.
- [5] R.N. Tubbs, *Lucky Exposures: Diffraction Limited Astronomical Imaging Through the Atmosphere* (Ph.D. thesis), Cambridge University, 2003.
- [6] Q. Du, I. Kopriva, Dependent component analysis for blind restoration of images degraded by turbulent atmosphere, *Neurocomputing* 72 (2009) 2682–2692.
- [7] D. Li, S. Simske, Atmospheric turbulence degraded-image restoration by kurtosis minimization, *IEEE Geosci. Remote Sens. Lett.* 6 (2009) 244–247.
- [8] X. Zhu, P. Milanfar, Removing atmospheric turbulence via space-invariant de-convolution, *IEEE Trans. Pattern Anal. Mach. Intell.* 35 (2013) 157–170.
- [9] M. Maheshwari, D. Krishnapriya, Satellite image enhancement and restoration-a review, *Int. J. Comput. Sci. Commun. Netw.* 6 (2016) 198–204.
- [10] H. Tan, X. Zeng, S. Niu, Q. Chen, Q. Sun, Multiscale de-blurring of remote sensing image based on regularization constraints, *J. Image Graph.* 20 (2015) 386–394.
- [11] O. Beltramo-Martin, C.M. Correia, et al., Focal-plane C n 2 (h) profiling based on single-conjugate adaptive optics compensated images, *Mon. Not. R. Astron. Soc.* 481 (2) (2018) 2349–2360.
- [12] R.J.L. Fétick, T. Fusco, et al., Physics-based model of the adaptive-optics-corrected point spread function-applications to the SPHERE/ZIMPOL and MUSE instruments, *Astron. Astrophys.* 628 (2019) A99.
- [13] X. Zhu, P. Milanfar, Stabilizing and de-blurring atmospheric turbulence, in: IEEE International Conference on Computational Photography, ICCP, 2011, pp. 1–8.
- [14] Y. Yuan, H. Lv, X. Lu, Semi-supervised change detection method for multi-temporal hyperspectral images, *Neurocomputing* 148 (2015) 363–375.
- [15] D. Wipf, H. Zhang, Revisiting Bayesian blind de-convolution, *J. Mach. Learn. Res.* 5 (2013) 3595–3634.
- [16] V. Soni, A.K. Bhandari, A. Kumar, et al., Improved sub-band adaptive thresholding function for denoising of satellite image based on evolutionary algorithms, *IET Signal Process.* 7 (2013) 720–730.
- [17] M. Sajid, K. Khurshid, Satellite image restoration using RLS adaptive filter and enhancement by image processing techniques, in: Symposium on Recent Advances in Electrical Engineering, RAEE, 2015, pp. 1–7.
- [18] L. Chao, H. Chen, et al., Research status of blind image restoration, *Chin. Opt.* 7 (2014) 68–78.
- [19] C.J. Schuler, M. Hirsch, S. Harmeling, B. Schölkopf, Learning to deblur, *IEEE Trans. Pattern Anal. Mach. Intell.* 38 (2016) 1439–1451.
- [20] D. Perrone, P. Favaro, A clearer picture of blind de-convolution, *Comput. Sci.* (2014).
- [21] Q. Chu, S. Jefferies, J.G. Nagy, Iterative wavefront reconstruction for astronomical imaging, *SIAM J. Sci. Comput.* 35 (2013) S84–S103.
- [22] M. Carbillat, Astronomical imaging atmospheric turbulence? adaptive optics!, *EAS Publ.* 59 (2013) 59–76.
- [23] S. Cho, S. Lee, Convergence analysis of MAP based blur kernel estimation, in: IEEE International Conference on Computer Vision, ICCV, 2018, pp. 4818–4826.
- [24] W.S. Lai, J.B. Huang, Z. Hu, N. Ahuja, M.H. Yang, A comparative study for single image blind de-blurring, in: IEEE Conference on Computer Vision and Pattern Recognition, CVPR, 2016, pp. 1701–1709.
- [25] S. Nah, T.H. Kim, K.M. Lee, Deep multi-scale convolutional neural network for dynamic scene de-blurring, in: IEEE Conference on Computer Vision and Pattern Recognition, CVPR, vol. 2, 2017.
- [26] J. Sun, W. Cao, Z. Xu, et al., Learning a convolutional neural network for non-uniform motion blur removal, in: IEEE Conference on Computer Vision and Pattern Recognition, CVPR, 2015, pp. 769–777.
- [27] L. Xu, X. Tao, J. Jia, Inverse kernels for fast spatial de-convolution, in: IEEE International Conference on Computer Vision, ICCV, 2014.
- [28] S. Liu, E. Johns, A.J. Davison, End-to-End multi-task learning with attention, in: IEEE Conference on Computer Vision and Pattern Recognition, CVPR, 2018.
- [29] J. Zhang, J. Pan, J. Ren, et al., Dynamic scene de-blurring using spatially variant recurrent neural networks, in: IEEE Conference on Computer Vision and Pattern Recognition, CVPR, 2018.
- [30] Y. Chen, W. Yu, T. Pock, On learning optimized reaction difmerge processes for effective image restoration, in: IEEE Conference on Computer Vision and Pattern Recognition, CVPR, 2015.
- [31] S. Lefkimiatis, Non-local color image denoising with convolutional neural networks, in: IEEE Conference on Computer Vision and Pattern Recognition, CVPR, 2017.
- [32] S. Guo, Z. Yan, K. Zhang, W. Zuo, L. Zhang, Toward convolutional blind denoising of real photographs, in: IEEE Conference on Computer Vision and Pattern Recognition, CVPR, 2018.
- [33] C. Dong, Y. Deng, C.C. Loy, X. Tang, Compression artifacts reduction by a deep convolutional network, in: IEEE International Conference on Computer Vision, ICCV, 2015.
- [34] J. Guo, H. Chao, Building dual-domain representations for compression artifacts reduction, in: IEEE International Conference on Computer Vision, ICCV, 2016.
- [35] Z. Wang, D. Liu, S. Chang, Q. Ling, Y. Yang, T.S. Huang, D3: Deep dual-domain based fast restoration of JPEG-compressed images, in: IEEE Conference on Computer Vision and Pattern Recognition, CVPR, 2016.
- [36] C. Dong, C.C. Loy, K. He, X. Tang, Image superresolution using deep convolutional networks, *IEEE Trans. Pattern Anal. Mach. Intell.* 38 (2016) 295–307.
- [37] Y. Tai, J. Yang, X. Liu, C. Xu, Memnet: A persistent memory network for image restoration, in: IEEE International Conference on Computer Vision, ICCV, 2017.
- [38] X. Wang, K. Yu, C. Dong, C.C. Loy, Recovering realistic texture in image super-resolution by deep spatial feature transform, in: IEEE Conference on Computer Vision and Pattern Recognition, CVPR, 2018.

- [39] J. Kim, J.K. Lee, K.M. Lee, Accurate image superresolution using very deep convolutional networks, in: IEEE Conference on Computer Vision and Pattern Recognition, CVPR, 2016.
- [40] Y. Tai, J. Yang, X. Liu, Image super-resolution via deep recursive residual network, in: IEEE Conference on Computer Vision and Pattern Recognition, CVPR, 2017, pp. 3147–3155.
- [41] J. Portilla, Blind non-white noise removal in images using Gaussian scale mixtures in the wavelet domain, in: Benelux Signal Processing Symposium, 2004.
- [42] J. Portilla, Full blind denoising through noise covariance estimation using Gaussian scale mixtures in the wavelet domain, in: International Conference on Image Processing, ICIP, vol. 2, 2004, pp. 1217–1220.
- [43] M. Lebrun, M. Colom, J.M. Morel, Multiscale image blind denoising, *IEEE Trans. Image Process.* 24 (2015) 3149–3161.
- [44] M. Lebrun, M. Colom, J.M. Morel, The noise clinic: a blind image denoising algorithm, *IPOL J.* 5 (2015) 1–54.
- [45] A. Foi, M. Trimeche, V. Katkovnik, K. Egiazarian, Practical poissonian-gaussian noise modeling and fitting for single-image raw-data, *IEEE Trans. Image Process.* 17 (2008) 1737–1754.
- [46] Z. Gao, C. Shen, C. Xie, Stacked convolutional auto-encoders for single space target image blind de-convolution, *Neurocomputing* 313 (2018) 295–305.
- [47] X. Liu, H. Ma, G. Ren, B. Qi, et al., Research on high-resolution imaging technology based on light field manipulation for a lenslet-based plenoptic camera, *Appl. Opt.* 57 (33) (2018) 9877–9886.
- [48] M.R. Chatterjee, A. Mohamed, F.S. Almehmadi, Secure free-space communication, turbulence mitigation, and other applications using acousto-optic chaos, *Appl. Opt.* 57 (10) (2018) C1–C13.
- [49] X. Xu, P. Yang, H. Xian, Y. Liu, Robust moving objects detection in long-distance imaging through turbulent medium, *Infrared Phys. Technol.* 100 (2019) 87–98.
- [50] R.V. Sreekanth, R.K. Banyal, R. Sridharan, A. Selvaraj, Measurements of atmospheric turbulence parameters at Vainu Bappu observatory using short-exposure CCD images, *Res. Astron. Astrophys.* 19 (5) (2019) 074.
- [51] A. Mohamed, M.R Chatterjee, Image intensity recovery with mitigation in the presence of gammagamma atmospheric turbulence using encrypted chaos, *Opt. Eng.* 58 (3) (2019) 036110.
- [52] K. Yu, C. Dong, L. Lin, C.C. Loy, Crafting a toolchain for image restoration by deep reinforcement learning, in: IEEE Conference on Computer Vision and Pattern Recognition, CVPR, 2018.
- [53] S.L.S. Gómez, C. González-Gutierrez, E.D. Alonso, et al., Experience with artificial neural networks applied in multi-object adaptive optics, *Publ. Astron. Soc. Pac.* 131 (1004) (2019) 108012.
- [54] J. Li, M. Zhang, D. Wang, S. Wu, Joint atmospheric turbulence detection and adaptive demodulation technique using the CNN for the OAM-FSO communication, *Opt. Express* 26 (8) (2018) 10494–10508.
- [55] D. Li, S. Xu, D. Wang, D. Yan, Phase diversity algorithm with high noise robust based on deep denoising convolutional neural network, *Opt. Express* 27 (16) (2019) 22846–22854.
- [56] A. Asensio Ramos, J. de la Cruz Rodriguez, A. Pastor Yabar, Real-time, multiframe, blind deconvolution of solar images, *Astron. Astrophys.* 620 (2018) A73.
- [57] L. Xu, J.S. Ren, C. Liu, J. Jia, Deep convolutional neural network for image de-convolution, *Adv. Neural Inf. Process. Syst.* (2014), 1790–1798.
- [58] M. Hradiš, J. Kotera, P. Zemcik, F. Šroubek, Convolutional neural networks for direct text de-blurring, in: British Machine Vision Conference, BMVC, vol. 10, 2015.
- [59] L. Xiao, J. Wang, W. Heidrich, M. Hirsch, Learning high-order filters for efficient blind de-convolution of document photographs, in: European Conference on Computer Vision, ICCV, 2016, pp. 734–749.
- [60] X. Mao, C. Shen, Y. Yang, Image restoration using very deep convolutional encoder-decoder networks with symmetric skip connections, 2016, arXiv preprint [arXiv:1603.09056v2](https://arxiv.org/abs/1603.09056v2).
- [61] J. Zhang, J. Pan, W.-S. Lai, R. Lau, M.H. Yang, Learning fully convolutional networks for iterative non-blind de-convolution, in: IEEE Conference on Computer Vision and Pattern Recognition, CVPR, 2017, pp. 6969–6977.
- [62] O. Kupyn, V. Budzan, M. Mykhailych, D. Mishkin, J. Matas, DeblurGAN: blind motion de-blurring using conditional adversarial networks, 2017, arXiv preprint [arXiv:1711.07064](https://arxiv.org/abs/1711.07064).
- [63] R. Gal, N. Kiryati, N. Sochen, Progress in the restoration of image sequences degraded by atmospheric turbulence, *Pattern Recognit. Lett.* 48 (2014) 8–14.
- [64] K. Simonyan, A. Zisserman, Very deep convolutional networks for large-scale image recognition, in: IEEE Conference on Computer Vision and Pattern Recognition, CVPR, 2015.
- [65] K. He, X. Zhang, S. Ren, J. Sun, Deep residual learning for image recognition, in: IEEE Conference on Computer Vision and Pattern Recognition, CVPR, 2016, pp. 770–778.
- [66] C. Szegedy, W. Liu, Y. Jia, P. Sermanet, S. Reed, D. Anguelov, D. Erhan, V. Vanhoucke, A. Rabinovich, Going deeper with convolutions, in: IEEE Conference on Computer Vision and Pattern Recognition, CVPR, 2015.
- [67] K. Zhang, Z. Wang, Y. Chen, D. Meng, L. Zhang, Beyond a Gaussian denoiser: residual learning of deep cnn for image denoising, *IEEE Trans. Image Process.* 26 (2017) 3142–3155.
- [68] C. Wen, R. Xu, T. Men, Atmosphere turbulence blurred image restoration based on atmosphere coherent length, *Acta Opt. Sin.* 34 (2014) 6–13.
- [69] K. Zhang, Z. Wang, S. Gu, L. Zhang, Learning deep CNN denoiser prior for image restoration, in: IEEE Conference on Computer Vision and Pattern Recognition, CVPR, 2017.